

# Determination of the electronic structure of bilayer graphene from infrared spectroscopy results

L. M. Zhang, Z. Q. Li, D. N. Basov, and M. M. Fogler  
University of California San Diego, 9500 Gilman Drive, La Jolla, California 92093

Z. Hao and M. C. Martin  
Advanced Light Source Division, Lawrence Berkeley National Laboratory, Berkeley, California 94720  
(Dated: September 3, 2018)

We present an experimental study of the infrared conductivity, transmission, and reflection of a gated bilayer graphene and their theoretical analysis within the Slonczewski-Weiss-McClure (SWMc) model. The infrared response is shown to be governed by the interplay of the interband and the intraband transitions among the four bands of the bilayer. The position of the main conductivity peak at the charge neutrality point is determined by the interlayer tunneling frequency. The shift of this peak as a function of the gate voltage gives information about less known parameters of the SWMc model, in particular, those responsible for the electron-hole and sublattice asymmetries. These parameter values are shown to be consistent with recent electronic structure calculations for the bilayer graphene and the SWMc parameters commonly used for the bulk graphite.

PACS numbers: 81.05.Uw, 78.30.Na, 78.20.Bh

## I. INTRODUCTION

Since the monolayer graphene was isolated<sup>1</sup> and shown to exhibit the quantum Hall effect<sup>2,3</sup> a few years ago, ultrathin carbon systems have attracted tremendous attention.<sup>4</sup> Their electron properties are quite unique. Monolayer graphene has a vanishing Fermi point at the Brillouin zone corner and low energy quasiparticles with a linear spectrum,  $\varepsilon(\mathbf{k}) = \pm v|\mathbf{k}|$ , which obey a massless Dirac equation. Here  $\mathbf{k}$  is the deviation of the crystal momentum from the Brillouin zone corner ( $K$  point),  $v = (3/2)\gamma_0 a/\hbar$  is the quasiparticle velocity,  $\gamma_0$  is the nearest-neighbor hopping parameter, and  $a = 1.42 \text{ \AA}$  is the carbon-carbon distance. Graphene is the basic building block of other types of carbon materials. Indeed, the first calculation of its band structure by Wallace<sup>5</sup> was motivated by his studies of graphite. Extending that work, Slonczewski and Weiss,<sup>6</sup> McClure,<sup>6,7</sup> and others<sup>8</sup> have developed the now commonly used Slonczewski-Weiss-McClure (SWMc) model for the low-energy electron properties of graphite. This model, which is equivalent to a tight-binding model with seven parameters,<sup>9</sup> has proven to be a very useful analytical tool. It permitted theoretical calculations of a vast number of properties of graphite, including its diamagnetic susceptibility, de Haas-van Alfvén effect, magneto-optical response, cyclotron resonance, and so on. These properties were actively studied experimentally until the late 70's and lead to accurate estimates of the principal SWMc parameters,  $\gamma_0$  through  $\gamma_3$ . Still, it proved challenging to unambiguously determine the remaining three SWMc constants  $\gamma_4$ ,  $\gamma_5$ , and  $\Delta$ , which are measured in tens of meV. For illustration, in Table I we list inequivalent parameter sets from the latest original sources, Refs. 10 and 11. Subsequently, the issue was further confounded by numerous misprints in reference books and reviews.<sup>12</sup> The density-functional theory calculations,<sup>13,14,15</sup> which nor-

mally have accuracy of  $\sim 0.1 \text{ eV}$  for quasiparticle dispersion, have not yet settled this discrepancy.

In view of the reinvigorated interest to graphene, it has become an important question to obtain the SWMc constants for a few layer graphene and also to compare them with those for bulk graphite. Thus, some difference between the graphite and a graphene bilayer was recently reported, based on the analysis of Raman scattering.<sup>16</sup> Several *ab initio* calculations of these parameters for the bilayer have also been done.<sup>17,18,19,20,21</sup> Unfortunately, they have not explicitly discussed the less accurately known SWMc parameters.

The bilayer is a system intermediate between graphene and bulk graphite. Its lattice structure (for the case of the Bernal or AB stacking) is illustrated in Fig. 1(a). The corresponding band structure,<sup>23,24,25</sup> shown in Fig. 1(b), consists of four bands. These bands arise from splitting and hybridization of the Dirac cones of the individual layers by the interlayer hopping matrix element  $\gamma_1$  and by the electrostatic potential difference  $V$  between the two layers.<sup>23,26</sup> The latter can be controlled experimentally by varying the voltage  $V_g$  of a nearby metallic gate<sup>27,28</sup> or by doping.<sup>29</sup> This degree of tunability makes the bilayer graphene an extremely interesting material for both fundamental study and applications.

In this paper we show that  $\gamma_1$ ,  $v_4 \equiv \gamma_4/\gamma_0$ , and  $\Delta$  can be *directly* extracted from the dynamical conductivity measured in zero magnetic field. This is in contrast to the bulk graphite where determination of the SWMc constants was never straightforward and almost invariably required the use of strong magnetic fields.

The dynamical conductivity  $\sigma(\Omega)$  is determined by the six possible transitions among the four bands, see Fig. 1(c). They have energies of the order of a few  $10^{-1} \text{ eV}$ , which is in the infrared optical range. Recently, experimental measurements of the infrared response of the bilayers have been carried out by our<sup>30</sup> and other<sup>31,32</sup>

TABLE I: The SWMc parameters (in eV) according to previous and present work. The numbers in parentheses are the reported accuracy of the trailing decimals. The “Exp” and “DFT” stand for experiment and density functional theory, respectively.

SWMc parameter	Graphene bilayer			Graphite, early work				Graphite, recent work	
	Pres. work	Exp <sup>a</sup>	DFT <sup>b</sup>	Exp <sup>c</sup>	Exp <sup>d</sup>	DFT <sup>e</sup>	DFT <sup>f</sup>	Exp <sup>g</sup>	DFT <sup>h</sup>
$\gamma_0$	3.0 <sup>i</sup>	2.9	2.6	3.16(5)	3.11	2.92	2.598(15)		
$\gamma_1$	0.40(1)	0.30	0.3	0.39(1)	0.392	0.27	0.364(20)		
$\gamma_2$	0.0 <sup>j</sup>	0.0 <sup>j</sup>	0.0 <sup>j</sup>	-0.020(2)	-0.0201	-0.022	-0.014(8)		
$\gamma_3$	0.3 <sup>i</sup>	0.10	0.3	0.315(15)	0.29	0.15	0.319(20)		
$\gamma_4$	0.15(4)	0.12		0.044(24)	0.124	0.10	0.177(25)		
$\gamma_5$	0.0 <sup>j</sup>	0.0 <sup>j</sup>	0.0 <sup>j</sup>	0.038(5)	0.0234	0.0063	0.036(13)		
$\Delta$	0.018(3)		0.01 <sup>k</sup>	-0.008(2)	-0.0049	0.0079	-0.026(10)	<0.01 <sup>l</sup>	-0.037 <sup>m</sup>
$\Delta' = \Delta - \gamma_2 + \gamma_5$	0.018(3)		0.01 <sup>k</sup>	0.037(5)	0.0386	0.0362	0.024(18)		

<sup>a</sup>L. M. Malard *et al.*, Phys. Rev. B **76**, 201401 (2007).<sup>16</sup>

<sup>b</sup>H. Min, B. R. Sahu, S. K. Banerjee, and A. H. MacDonald, Phys. Rev. B **75**, 155115 (2007).<sup>20</sup>

<sup>c</sup>M. S. Dresselhaus and G. Dresselhaus, Adv. Phys. **30**, 139 (1981).<sup>10</sup>

<sup>d</sup>R. O. Dillon, I. L. Spain, and J. W. McClure, J. Phys. Chem. Solids **38**, 635 (1977).<sup>11</sup>

<sup>e</sup>R. C. Tatar and S. Rabii, Phys. Rev. B **25**, 4126 (1982).<sup>13</sup>

<sup>f</sup>J.-C. Charlier, X. Gonze, and J.-P. Michenaud, Phys. Rev. B **43**, 4579 (1991).<sup>14</sup>

<sup>g</sup>M. Orlita *et al.*, Phys. Rev. Lett. **100**, 136403 (2008).<sup>22</sup>

<sup>h</sup>A. Grüneis *et al.*, Phys. Rev. Lett. **100**, 037601 (2008).<sup>15</sup>

<sup>i</sup>This value cannot be very accurately found from our analysis and is instead adopted from the literature.

<sup>j</sup>Physically irrelevant in the bilayer but should be set to zero for calculating  $\Delta'$  from  $\Delta$ .

<sup>k</sup>Our estimate based on digitizing band dispersion graphs published in Refs. 18,19,20,21.

<sup>l</sup>Absolute value only.

<sup>m</sup>The negative sign (omitted in Ref. 15) is required for consistency with the conventional definition<sup>7</sup> of  $\Delta$ .

groups. Below we identify and explain the key findings of these experiments based on how different combinations of the interband transitions are either activated or suppressed by the Pauli exclusion principle. Our theory enables us to reach a quantitative agreement with the experiment using SWMc  $\gamma_0$ ,  $\gamma_1$ ,  $\gamma_4$ , and  $\Delta$ , and also the phenomenological broadening constant  $\Gamma$  as adjustable parameters. The values of the SWMc parameters that give the best fit are given in the second column of Table I. Note that the next-nearest layer hopping parameters  $\gamma_2$  and  $\gamma_5$  are irrelevant for the bilayer. The parameter  $\gamma_3$  cannot be reliably estimated from these particular experiments because it has an effect similar to the simple broadening ( $\Gamma$ ) in the range of carrier concentrations suitable for our analysis.

Previous theoretical studies of the optical conductivity of bilayer graphene<sup>24,25,33,34,35</sup> used a simplified model in which only  $\gamma_0$  and  $\gamma_1$  were taken into account. This model successfully explains the major features of  $\sigma(\Omega)$  as well as its dependence on the gate voltage  $V_g$ , and we qualitatively summarize it as follows. Conduction and valence bands are symmetric. In the absence of the electrostatic potential difference  $V$  between the layers the two conduction (valence) bands have the same shape and are shifted by  $\gamma_1$ . Except the range of very small momenta  $k$ , their shape remain nearly identical even in the presence of a finite  $V$ . As a result, there is a high optical density of states for transitions between the two pairs of bands at frequency  $\gamma_1/\hbar$ , which gives rise to a sharp peak in the real part of the conductivity  $\text{Re}\sigma(\Omega)$  at  $\Omega = \gamma_1/\hbar \approx 3200 \text{ cm}^{-1}$  (using  $\gamma_1 = 0.40 \text{ eV}$ ). Other

transitions give more gradually varying contributions to  $\text{Re}\sigma(\Omega)$ , eventually leading to the asymptotic “universal” value<sup>24,25,33,34,35,36,37</sup>  $\sigma = e^2/2\hbar$  at high frequency (which is twice the value for the monolayer<sup>38</sup>). Finally, in real graphene systems the conductivity features are never sharp because of a finite lifetime due to, e.g., disorder scattering. This broadens the peaks and can also merge together several features that are close in energy, see Fig. 2.

Our recent infrared experiments<sup>30</sup> as well as measurements by another group<sup>32</sup> have largely confirmed this picture but also found features that cannot be explained within this simple model. In particular, the conductivity peaks on the electron and the hole sides are displaced in energy from  $\gamma_1$  by about 10% in opposite directions. [Electron and hole doping is identified with, respectively, positive and negative  $\delta V = V_g - V_{\text{CN}}$ , where  $V_{\text{CN}}$  is the gate voltage at which the bilayer is tuned to the charge-neutrality (CN) point.]

In order to investigate the origin of these features in this paper we carry out a combined experimental-theoretical study of the infrared response of a bilayer graphene. We attribute the observed electron-hole asymmetry to the effect of  $\gamma_4$  and  $\Delta$ . We find that including these parameters is essential for a more accurate discussion of  $\sigma(\Omega)$  of the bilayer. Besides differences in the optical response,  $\gamma_4$  and  $\Delta$  also make effective masses for electrons and holes unequal,<sup>39</sup> in agreement with the findings from the Raman scattering.<sup>16</sup>

In our experiments, we have measured the optical reflection  $R(\Omega, V_g)$  and transmission  $T(\Omega, V_g)$  as a function

of the frequency  $\Omega$  and the gate voltage  $V_g$ . From  $R$  and  $T$  we extracted the real and imaginary part of the conductivity using a commercial software package. Some of these experimental results were reported previously.<sup>30</sup>

In this paper we present more extensive experimental data and we also compute the same three quantities —  $\sigma$ ,  $R$ , and  $T$  — theoretically. The calculation requires accounting for the interplay of several physical phenomena: (a) electrostatic charging of the layers (b) their dynamical conductivity, (c) disorder, and (d) the optical properties of the environment (sample, substrate, and the gate). Each of these ingredients has been studied in the past.<sup>24,25,27,33,34,35,40,41</sup> Here we carry out all these calculations in a single paper albeit we include disorder broadening in a very simple way. This enables us to directly compare our theoretical results with the measurements.

The remainder of the paper is organized as follows. In Sec. II we summarize our results. Theoretical derivation is outlined in Sec. III. Section IV contains comparison of the theory and experiment, discussion, and conclusions.

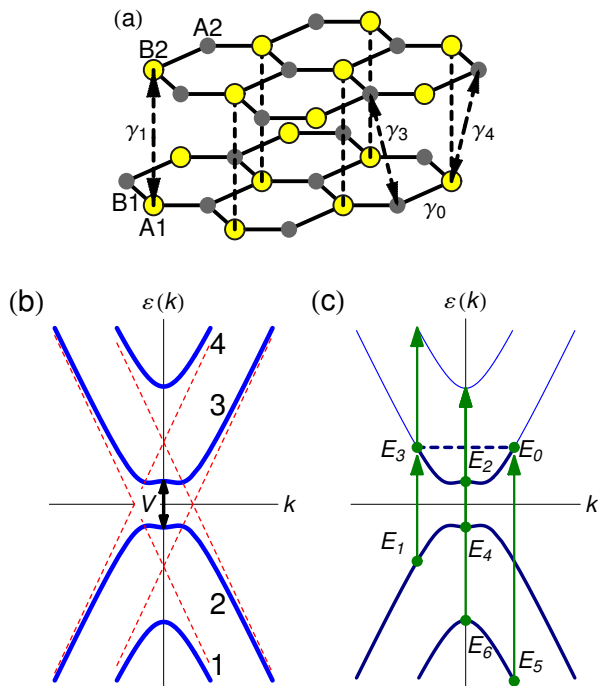


FIG. 1: (Color online) (a) Crystal structure of the graphene bilayer with the relevant SWMc hopping parameters shown. (b) Band structure of a biased bilayer (lines), which can be considered as hybridization of two shifted Dirac cones (dots). Numbers on the right label the four bands. (c) Examples of the allowed optical transitions for the chemical potential indicated by the dashed line. Occupied states are shown by the thicker lines. The dots and the arrows mark the initial and the final states, respectively, of the transitions that produce features at frequencies  $E_j$ ,  $j = 1, 2, \dots, 6$  in Fig. 2(a) below.  $E_0$  is the intraband transition (Drude peak).

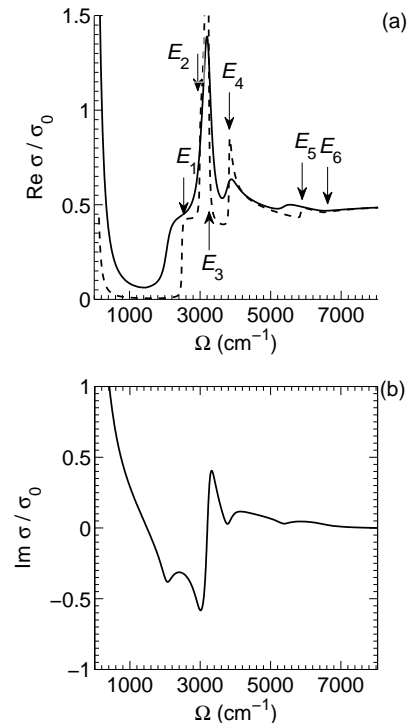


FIG. 2: (a) Real and (b) imaginary part of conductivity in units of  $\sigma_0 = e^2/h$  for the gate voltage  $\delta V = -100$  V. The solid curves are for broadening  $\Gamma = 0.02\gamma_1$ . The dashed curve is for  $\Gamma = 0.002\gamma_1$ .

Some calculational details are relegated to the Appendix.

## II. RESULTS

To measure the optical response of the bilayer we employed synchrotron infrared radiation, as described previously.<sup>30,42</sup> Understandably, the two-atom thick sample has a rather small optical signal. The quantity which can be extracted most reliably from the current experiments is the relative transmission  $T(\Omega, V_g)/T(\Omega, V_{CN})$  and reflection  $R(\Omega, V_g)/R(\Omega, V_{CN})$ . All measurements were done at the temperature of 45 K. The data for the largest  $|\delta V| = |V_g - V_{CN}|$  are depicted in Fig. 3. The main feature in the relative transmission spectra is a small but clearly visible dip around  $\Omega = 3200$  cm<sup>-1</sup>. Away from the dip, the relative transmission is slightly higher than unity. The relative reflection spectra are characterized by a dip-peak structure. Transmission and reflection spectra are asymmetric between positive and negative  $\delta V$ , which correspond, respectively, to doping of electrons and holes in bilayer graphene.

From the transmission and reflection data, we extracted the optical conductivity.<sup>30,42,43</sup> The dominant feature in the conductivity spectra is a strong peak at  $\Omega \approx 3200$  cm<sup>-1</sup>, see Fig. 4(c). Below the main peak, we observed a broadened threshold feature, which shifts sys-

tematically with  $\delta V$ . The most intriguing observation is again the electron-hole asymmetry in the optical conductivity. For instance, the frequencies of the main peak in  $\text{Re}\sigma(\Omega)$  and its voltage dependence are noticeably different for electrons and holes, see Fig. 4(c). Also, while the peak is quite symmetric at large positive voltages, at high negative  $\delta V$ , it is not. The most probable reason is the existence of a secondary peak at a slightly larger  $\Omega$ , see below.

On the theory side, we calculated  $\sigma$ ,  $T$ , and  $R$ , using the SWMc constants and  $\Gamma$  as adjustable parameters. Results for the conductivity are shown in Fig. 4(b). The reflection and transmission are plotted in Fig. 3. The calculational parameters were adjusted to reproduce the frequency positions and widths of the main features of the experimental data. Interestingly, in this way of fitting, it was not possible to achieve an equally good agreement for the vertical scale of the observed features. Still their qualitative trend as a function of  $\delta V$  is reproduced well.

Both in experiment and in calculations the carrier concentrations are always smaller than the characteristic value  $n_0$  given by

$$n_0 = \frac{\gamma_1^2}{\hbar^2 v^2} = 3.7 \times 10^{13} \text{ cm}^{-2}. \quad (1)$$

Here and below we assume that  $\gamma_0 = 3.0 \text{ eV}$ , which corresponds to  $v = (3/2)\gamma_0 a/\hbar = 1.0 \times 10^8 \text{ cm/s}$ . (Based on other results in the literature, this value should be accurate to about 10%.) At concentrations  $|n| < n_0$  the high energy bands 1 and 4 have no free carriers and  $\text{Re}\sigma(\Omega)$  has a pronounced peak at  $\Omega \approx 3200 \text{ cm}^{-1}$ . As explained above, this feature corresponds to transition between band pairs that are nearly parallel: bands 3 and 4 for  $\mu > 0$  or bands 1 and 2 for  $\mu < 0$ , see Fig. 1.

The evolution of the infrared response with  $V_g$  can be understood as follows. As the gate voltage deviates further away from  $V_{\text{CN}}$ , the electron concentration

$$n = C_b \delta V / e \quad (2)$$

and the chemical potential  $\mu$  increase by the absolute value. Here  $C_b$  is the capacitance between the bilayer and the gate. As a result of an increased  $|n|$ , the peak become more pronounced. Simultaneously, near the higher frequency side of the peak a depletion of conductivity develops. One can say that the optical weight is increasingly transferred from the high frequencies to the  $\gamma_1$  peak. Larger conductivity is directly associated with decreased optical transmission. Therefore one observes an increasing dip in the transmission near  $\gamma_1$  and a higher transmission at higher  $\Omega$ , see Fig. 3. Similar features appear in the reflection but they are more difficult to interpret as they are also affected by  $\text{Im}\sigma(\Omega)$ .

Very important for our analysis are the aforementioned small shifts in the position of the  $\gamma_1$  peak as a function of  $\delta V$ . Within the SWMc model, their origin is as follows. In the absence of broadening, the peak arises from the absorption in the range of frequencies,  $E_2 < \hbar\Omega < E_3$ , see

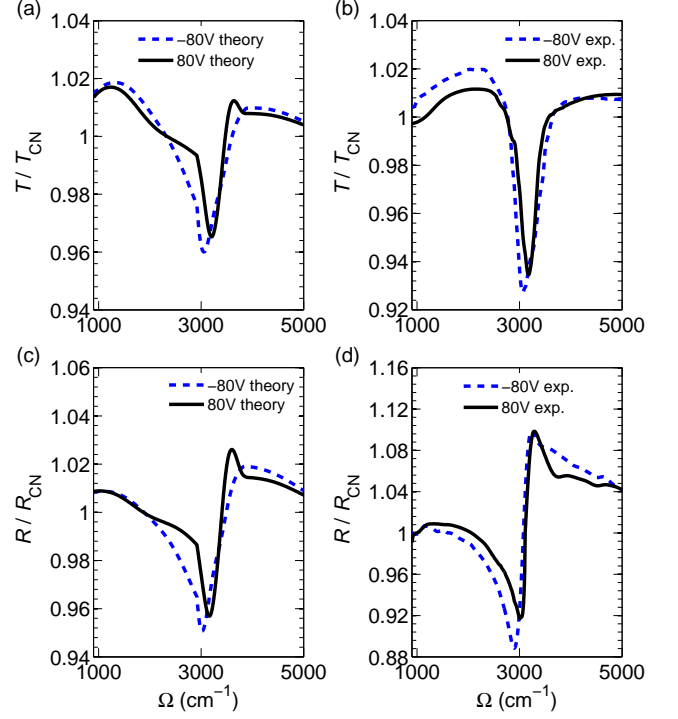


FIG. 3: (Color online) Relative transmission: (a) theory (b) experiment. Relative reflection: (c) theory (d) experiment. The solid line is for electrons,  $\delta V \approx +80 \text{ V}$ . The dashed line is for holes,  $\delta V \approx -80 \text{ V}$ . The experimental uncertainties are  $\sim 0.002$  (0.2%) at  $\Omega$  near  $3000 \text{ cm}^{-1}$  and  $\sim 0.5\%$  at high frequency.

Figs. 1 and 2. Since the optical weight at  $E_3$  is higher, the conductivity peak occurs at energy  $E_3$ . However, if the broadening is large enough, the optical weight becomes distributed more uniformly, and the peak position moves to the midpoint of  $E_2$  and  $E_3$ , see Fig. 5. Energies  $E_2$  and  $E_3$  themselves vary with the gate voltage (or  $n$ ). For positive  $\delta V$  (positive  $n$ ),  $E_2 \equiv E_2^+$  is the energy difference between the bands 3 and 4 at  $k = 0$ . The energy  $E_3 \equiv E_3^+$  is the corresponding difference at  $k = k_F$ , where

$$k_F = \text{sign}(n) \sqrt{\pi|n|} \quad (3)$$

is the Fermi momentum. For  $\delta V < 0$  we denote  $E_2$  and  $E_3$  by, respectively,  $E_2^-$  and  $E_3^-$  and they are computed using the bands 1 and 2 instead of 3 and 4.

From the band structure,<sup>24,25</sup> we can find the following approximate expressions valid for  $n \ll n_0$ :

$$\begin{aligned} E_2^\pm &\simeq \gamma_1 - \frac{V}{2} \pm \Delta, \\ E_3^\pm &\simeq \gamma_1 \sqrt{1 + \frac{2\pi|n|}{n_0}} - \sqrt{\frac{V^2}{4} + \left(\frac{\pi\gamma_1 n}{n_0}\right)^2} \\ &\quad \pm \Delta \mp 2(2v_4\gamma_1 + \Delta) \frac{\pi|n|}{n_0}. \end{aligned} \quad (4) \quad (5)$$

Here  $V = V(n)$  as well as the chemical potential  $\mu = \mu(n)$  are determined self-consistently by the electrostatics

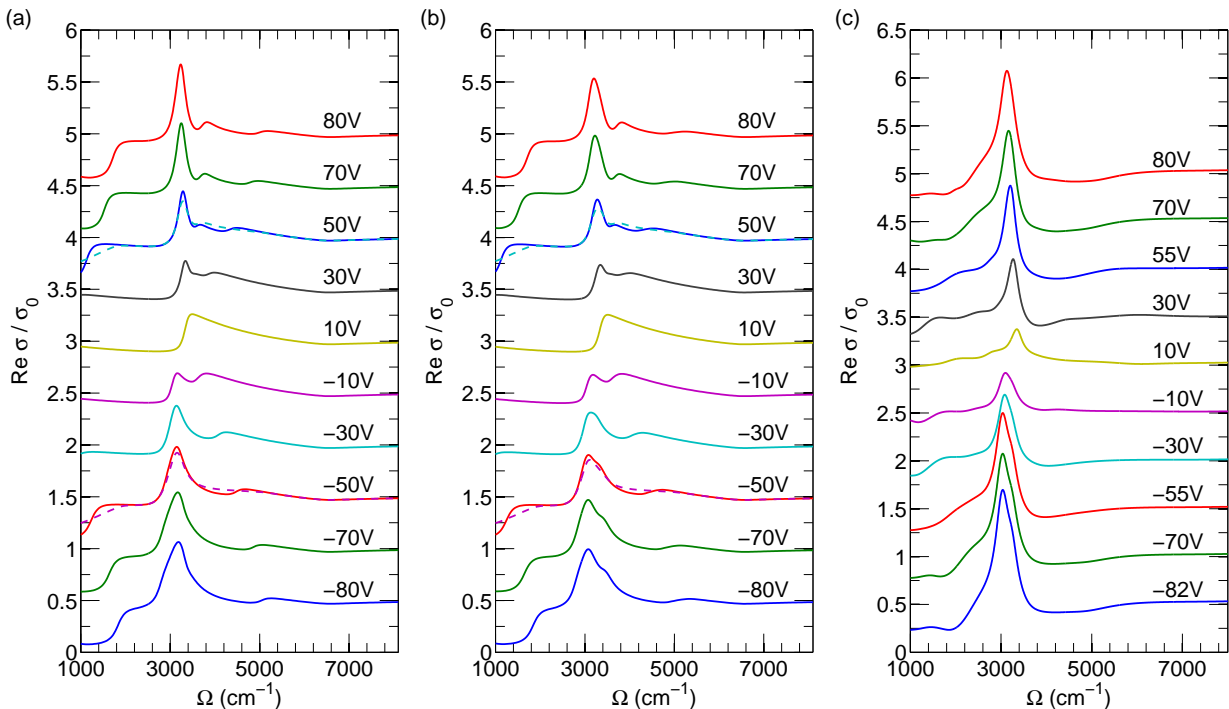


FIG. 4: (Color online) (a), (b) Theoretical and (c) experimental results for the conductivity  $\text{Re } \sigma$ , in units of  $\sigma_0 = 4e^2/\hbar$ , as a function of frequency  $\Omega$ . The deviation  $\delta V$  of the gate voltage from the charge neutrality point is indicated next to each curve. For clarity, the curves are offset vertically by  $0.5\sigma_0$  from one another. The SWMc parameters for plot (b) are given in Table I. In (a) they are the same, except  $\gamma_3$  is set to zero. The dashed curves superimposed on the  $\delta V = +50\text{ V}$  ( $-50\text{ V}$ ) traces in (a) and (b) are the arithmetic means of all the positive (negative)  $\delta V$  curves. Their significance is discussed in Sec. IV. The estimated uncertainty of the measured  $\text{Re } \sigma$  is  $0.125\sigma_0$  at  $\Omega \sim 8000\text{ cm}^{-1}$  and  $0.0625\sigma_0$  at  $\Omega \sim 3000\text{ cm}^{-1}$ .

of the system,<sup>40</sup> see Sec. III. These equations indicate that the parameters primarily responsible for electron-hole asymmetry are  $\gamma_4$  and  $\Delta$ .

Parameter  $\Delta$  is the difference of the on-site electron energies of the A and the B sites<sup>8,9</sup> [the stacked and unstacked sublattices, respectively, see Fig. 1(a)]. It has two effects: first, it lifts the  $k = 0$  energy for bands 1 and 4; second, it adds a  $k$  dependent perturbation to the two band dispersion. Parameter  $v_4 = v\gamma_4/\gamma_0$  of dimension of velocity characterizes hopping between a stacked atom and its three unstacked neighbors of its stacking partner. It also introduces difference between the valence and conduction bands. To the leading order in  $k$ , this hopping shifts the two middle bands (2 and 3) upward by a term proportional to  $v_4 k^2$  and shifts the two outer bands (1 and 4) downward by the same amount. These effects of  $\Delta$  and  $v_4$  are illustrated in Fig. 6.

Additional electron-hole asymmetry can in principle come from extrinsic sources, e.g., charged impurities that can be present on or between the layers. Besides creating a finite  $V_{\text{CN}}$ , these charges also move  $V = 0$  point away from the charge neutrality point  $n = 0$ . To the first approximation,<sup>40</sup> this introduces an offset of the inter-layer bias:  $V(n) \rightarrow V(n) + V_0$ . However, our calculations suggest that for reasonable  $V_0$  this effect has a smaller

influence on the electron-hole asymmetry of the optical response than  $\Delta$  and  $\gamma_4$ .

Based on the above discussion, we can predict qualitatively how the position of the main conductivity peak should vary as a function of  $\delta V$ . For example, on the electron side, and for  $v_4 > 0$ , the peak should move to lower frequencies as  $\delta V$  increases. Alternatively, this can be seen from Fig. 6: the top two bands move closer to each other as  $k = k_F$  increases.

For the quantitative analysis, we use a full numerical calculation of  $\sigma$  and  $T$ , which is discussed in Sec. III below. It demonstrates that for the case of small  $\Gamma$  the energy  $E_3$  is indeed in a good agreement with the computed peak position  $\Omega_0$ . However, the broadening observed in experiments<sup>30,31,32</sup> is appreciable, in which case the formula  $\Omega_0 = (E_2 + E_3)/2$  is more accurate. Of course, for fairly large  $\Gamma$  other nearby transitions,  $E_1$  and  $E_4$ , start to influence the lineshape of the main peak. This is especially noticeable on the hole side, where the  $E_4$ -peak is right next to the main one. In the calculations this two-peak structure is unmistakable, see Fig. 4(b). In the experiment, where the main peak is for some reason strongly enhanced compared to the calculation, the  $E_4$  peak is somewhat disguised. As pointed out by Kuzmenko,<sup>32</sup> the difference between  $E_4$  and  $E_2$  can in prin-

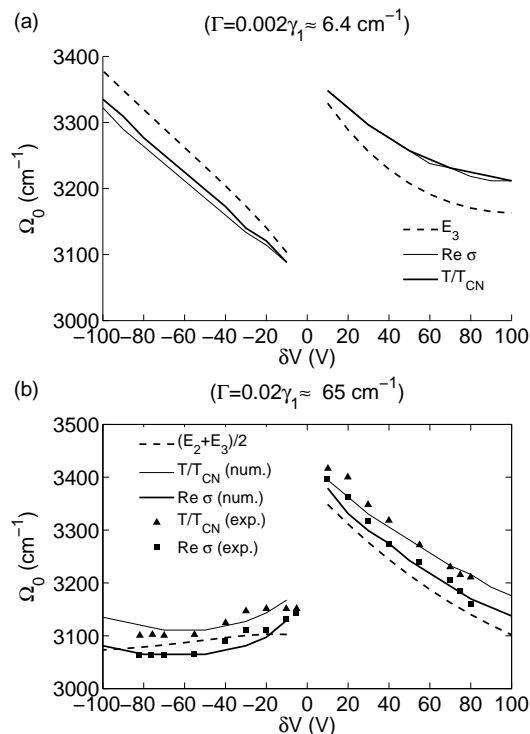


FIG. 5: Position of the  $\gamma_1$  peak *vs.* gate voltage for the two values of the broadening: (a)  $\Gamma = 0.02\gamma_1$  and (b)  $\Gamma = 0.002\gamma_1$ . The solid lines are our numerical results from the conductivity; the thick lines are from the relative transmission. The dashed lines show  $E_3$  and  $(E_2 + E_3)/2$  in the cases (a) and (b), respectively. The SWMc parameters used in the calculation are listed in the first column of Table I, except in (a)  $\gamma_3$  is set to zero. The symbols are the peak positions determined from the measured conductivity (squares) and transmission (triangles).

ciple provide a direct spectroscopic measurement of the energy gap  $V$ .

For detailed comparison with experiment we use our numerical results rather than Eqs. (4) and (5). Fitting them to the data, see Fig. 5, we have obtained estimates of  $\gamma_1$ ,  $\gamma_4$ , and  $\Delta$  listed in Table I. This fitting procedure proved to be very straightforward. For example,  $\Delta$  is determined mostly by the splitting of the peak positions on the electron and the holes sides of the charge neutrality point. Parameter  $\gamma_1$  is essentially the average of the two. Finally,  $\gamma_4$  controls the slope of the  $\Omega_0(V_g)$  curves away from  $V_{\text{CN}}$ . Therefore, all these parameters can be uniquely determined.

In Table I we also list SWMc values suggested in prior literature. They mainly agree with ours for the principal SWMc parameters  $\gamma_0$  and  $\gamma_1$  but show some deviations for the more subtle quantities  $\gamma_4$  and  $\Delta$  we have been discussing here. Possible reasons for these differences are given in Sec. IV.

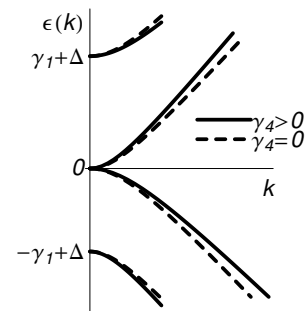


FIG. 6: The effect of  $\gamma_4$  and  $\Delta$  on the band structure. Parameter  $\Delta$  raises the bands 1 and 4. The interlayer neighbor hopping term  $\gamma_4$  gives a contribution quadratic in  $k$  opposite in sign for the conduction and the valence bands. The solid (dashed) lines are the bands with positive (zero) value of  $\gamma_4$ .

### III. DERIVATION

#### A. Band structure

The bilayer is two monolayers stacked together, see Fig. 1(a). In the bulk graphite the preferential stacking is the AB (Bernal) one, such that only one sublattice of each layer is bonded to each other. In order to achieve agreement with experiments,<sup>30</sup> we have to assume that in the bilayer the stacking is the same. We use the basis  $\{\Psi_{A1}, \Psi_{B1}, \Psi_{B2}, \Psi_{A2}\}$ , where the letter stands for the sublattice label and the number represents the layer index. In this basis the SWMc tight-binding Hamiltonian for the bilayer becomes<sup>25</sup>

$$\mathbf{H} = \begin{pmatrix} -\frac{V}{2} + \Delta & \phi & \gamma_1 & -v_4\phi^* \\ \phi^* & -\frac{V}{2} & -v_4\phi^* & v_3\phi \\ \gamma_1 & -v_4\phi & \frac{V}{2} + \Delta & \phi^* \\ -v_4\phi & v_3\phi^* & \phi & \frac{V}{2} \end{pmatrix}, \quad (6)$$

where  $\phi = -i(k_x + ik_y)$  and  $(k_x, k_y)$  is the deviation of the quasimomentum from the  $K$  point.

Given  $V$ , it is easy to obtain the four band energies  $\epsilon_\alpha(k)$  and the corresponding eigenstates  $|\alpha, \mathbf{k}\rangle$  numerically. However, as mentioned in Sec. II,  $V$  should be determined self-consistently as a function of  $V_g$ , or equivalently, the total carrier concentration  $n$ . The algorithm for doing so is given next.

#### B. Electrostatics

As discussed in the literature,<sup>25,40</sup> the electric field of the gate has two major effects on the bilayer graphene.

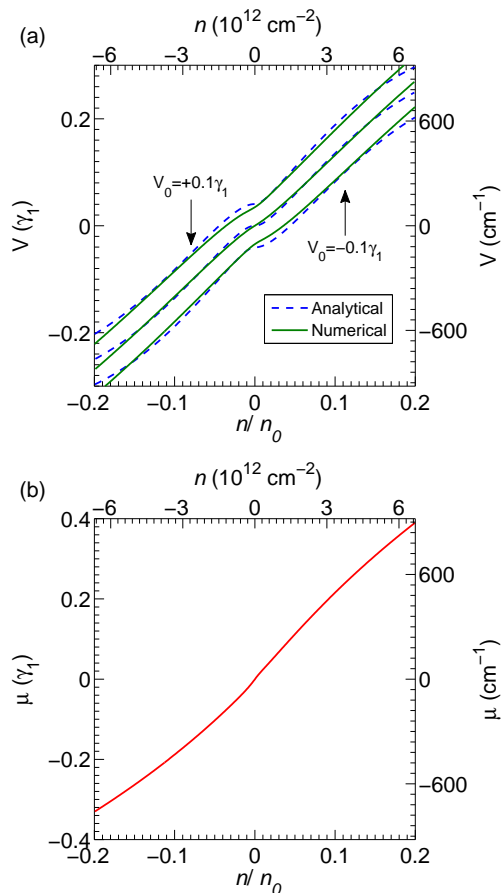


FIG. 7: (a) Interlayer bias  $V$  as a function of total density  $n$ . Three sets of curves correspond to (from top to bottom)  $V_0 = 0.1\gamma_1$ ,  $0$ , and  $-0.1\gamma_1$ . The dashed lines are computed from Eq. (12). (b) Chemical potential *vs.*  $n$  for  $V_0 = -0.1\gamma_1$ .

First, it modifies the bands by introducing a potential difference between the layers and as a consequence opens up the energy gap. Second, it induces charge carriers. Electric field of the charged impurities can play a similar role: it creates a layer asymmetry  $V_0$  and opens a gap at the charge neutral point much like an external gate. But the more important effect of the impurities is presumably the broadening of the electron energy states, which we describe by a phenomenological constant  $\Gamma$ . For example, if the impurities are distributed symmetrically between the two layers, then  $V_0$  is zero but  $\Gamma$  is still finite. We assume  $\Gamma$  to be real and independent of energy, momentum, or a band index. This is certainly a very rudimentary treatment of disorder compared to, e.g., self-consistent schemes.<sup>25,36,44</sup> However, since the source of disorder in graphene is still debated, we think that this simple approach is adequate for our purposes as long as  $\Gamma$  is treated as another adjustable parameter.

To compute  $V(n)$  and  $\mu(n)$  we set up a system of equations similar to those in Refs. 40 and 24. These equations capture the dominant Hartree term of the interaction but neglect exchange and correlation energies.<sup>20</sup> The first

equation is [cf. Eq. (2)]

$$n = n_t + n_b = C_b \delta V / e, \quad (7)$$

where  $n_t$  and  $n_b$  are the carrier concentrations of the top and bottom layers, and  $C_b$  is the capacitance to the gate. Second, the electrostatic potential difference between the two layers  $V$  is given by

$$V = \frac{4\pi e^2}{\kappa} (n_t - n_b) c_0, \quad (8)$$

where  $\kappa$  is the dielectric constant and  $c_0$  is the distance between the layers. Next, the Hamiltonian and hence the wavefunction and the layer density  $n_t$  and  $n_b$  depend on  $V$ . Therefore the quantities  $V$ ,  $n_t$ , and  $n_b$  must be solved for self-consistently. If the broadening  $\Gamma$  is neglected, this can be done analytically in the limit  $V, \mu \ll \gamma_1$ , which gives  $V \simeq \mathcal{V}(n, V_0)$ , where<sup>24,40</sup>

$$\mathcal{V}(n, V_0) = \frac{X\gamma_1 + V_0}{\Lambda^{-1} + |X| - \frac{1}{2} \ln |X|}, \quad X = \frac{\pi n}{n_0}, \quad (9)$$

$n_0$  is defined by Eq. (1), and  $\Lambda \equiv e^2 c_0 n_0 / (\pi \kappa \gamma_1)$  is the dimensionless strength of the interlayer screening. Using the typical parameter values, one estimates<sup>40</sup>  $\Lambda \sim 1$ , and so the interlayer screening is significant.<sup>20,40</sup>

For experimentally relevant broadening  $\Gamma \sim 0.02\gamma_1$ , the approximation leading to Eq. (9) is no longer accurate. Therefore, we computed the dependence of  $n_t$  and  $n_b$  on  $V$  numerically as follows. We first define the retarded Green's function  $\mathbf{G}^R$  by the analytic continuation  $\mathbf{G}^R(\varepsilon) = \mathbf{G}(\varepsilon \rightarrow \varepsilon + i\Gamma)$  of the following expression

$$\mathbf{G}(\varepsilon) = \sum_{\alpha=1}^4 \frac{1}{\varepsilon - \varepsilon_{\alpha}(k)} |\alpha, \mathbf{k}\rangle \langle \alpha, \mathbf{k}|. \quad (10)$$

Then we compute  $n_t$  from

$$n_t = - \int \frac{d^2k}{(2\pi)^2} \int_{-\infty}^{\mu} \frac{d\varepsilon}{\pi} \text{Im}[G_{11}^R(\mathbf{k}, \varepsilon) + G_{22}^R(\mathbf{k}, \varepsilon)], \quad (11)$$

using numerical quadrature. Similarly, the formula for  $n_b$  is obtained by replacing  $G_{11} + G_{22}$  with  $G_{33} + G_{44}$ .

The system of nonlinear equations (7), (8), and (11) is solved by an iterative procedure. For a given chemical potential  $\mu$  we start from some initial guess on  $V$ . Then we diagonalize the Hamiltonian and compute  $\mathbf{G}^R$ ,  $n_t$ , and  $n_b$ . Substituting them into Eq. (8), we get the value of  $V$  for the next iteration. (Actually, we use not this value directly but a certain linear combination of the new and old  $V$  to achieve convergence.) The iterations terminate when the values of  $V$  changes by less than a desired relative accuracy (typically,  $10^{-5}$ ). The results of these calculations are in a good agreement with Eq. (9) for  $\Gamma = 0$ , and so are not shown. On the other hand, the results for  $\Gamma = 0.02\gamma_1$ , which are plotted in Fig. 7, appreciably deviate from Eq. (9). The agreement greatly

improves (see Fig. 7) if instead of Eq. (9) we use, on heuristic grounds, the following formula:

$$V(n) = \mathcal{V}(n_*, V_0) - \mathcal{V}(n_\Gamma, 0), \quad (12)$$

$$n_* = \text{sign}(n) \sqrt{n^2 + n_\Gamma^2}, \quad n_\Gamma = \text{sign}(n) \frac{2\Gamma n_0}{\pi\gamma_1}. \quad (13)$$

### C. Dynamical conductivity

The above procedure enables us to compute  $V$  and  $n$  for a given chemical potential  $\mu$ . With the former deter-

mining the Hamiltonian and therefore its eigenstates, and the latter determining their occupancy, we can now compute the dynamical conductivity by the Kubo formula<sup>45</sup>

$$\sigma_{xx}(\Omega) = i \frac{\Pi_{xx}^R(\Omega) - \Pi_{xx}^R(0)}{\Omega + i0}, \quad (14)$$

where the polarization operator  $\Pi_{xx}^R(\Omega)$  is given by

$$\Pi_{xx}^R(\Omega) = ig \frac{e^2}{\hbar^2} \int \frac{d^2k}{(2\pi)^2} \int_{-\infty}^{\mu} \frac{d\varepsilon}{2\pi} \text{Tr} \{ \mathbf{v}_x [\mathbf{G}^R(\mathbf{k}, \varepsilon) - \mathbf{G}^A(\mathbf{k}, \varepsilon)] \mathbf{v}_x [\mathbf{G}^R(\mathbf{k}, \varepsilon + \Omega) + \mathbf{G}^A(\mathbf{k}, \varepsilon - \Omega)] \}. \quad (15)$$

In this equation  $g = 4$  is the spin-valley degeneracy of graphene,  $\mathbf{v}_x = \hbar^{-1} \partial \mathbf{H} / \partial k_x$  is the velocity operator, and  $\mathbf{G}^{R,A}$  at the retarded and the advanced Green's functions. Assuming again that the broadening is momentum and energy independent, these functions are obtained by the analytic continuation of  $\mathbf{G}$  in Eq. (10):  $\mathbf{G}^{R,A}(\varepsilon) = \mathbf{G}(\varepsilon \rightarrow \varepsilon \pm i\Gamma)$ . After some algebra, we find

$$\Pi_{xx}^R(\Omega) = ig \left( \frac{e}{\hbar} \right)^2 \int \frac{d^2k}{(2\pi)^2} \sum_{\alpha, \beta} |M_{\alpha\beta}(\mathbf{k})|^2 \sum_{\xi, \zeta = \pm 1} \xi K[\varepsilon_\beta(k) - i\Gamma\xi, \varepsilon_\alpha(k) - (i\Gamma + \Omega)\zeta], \quad (16)$$

where  $M_{\alpha\beta}(\mathbf{k}) = \langle \alpha, \mathbf{k} | \mathbf{v}_x | \beta, \mathbf{k} \rangle$  are the transition matrix elements and function  $K$  is defined by

$$K(z_1, z_2) = \frac{\ln(\mu - z_1) - \ln(\mu - z_2)}{2\pi(z_1 - z_2)} \quad (17)$$

with the branch cut for  $\ln z$  taken to be  $(-\infty, 0]$ .

For vanishing  $V$  and  $\Gamma$  the conductivity can be computed in the closed form, see Appendix B. For other cases, we evaluated it numerically. The results are shown in Figs. 2 and 4. To demonstrate agreement with previous theoretical calculations,<sup>24,25,33,35</sup> we present  $\sigma(\Omega)$  computed for a very small broadening  $\Gamma$  in Fig. 2. In this case one can easily identify all six transitions. As explained above, the sharp features at  $\Omega \approx 3200 \text{ cm}^{-1}$  are due to the high optical density of states at energies  $E_2 < \hbar\Omega < E_3$ . The other prominent feature at  $\Omega = 0$  is the intraband Drude peak. (Its height is related to the transport mobility.) In Fig. 4 the calculation is done for much larger  $\Gamma$  to match the experimental data. This Figure has been discussed in detail in Sec. II.

## IV. DISCUSSION

In this paper we presented a joint experimental and theoretical study of the infrared response of a bilayer graphene. Our results demonstrate a complex interplay

among various interband transitions and their disorder-induced broadening. Nevertheless, by means of a careful analysis, we have been able to explain the majority of the observed features within the conventional SWMc model. The corresponding SWMc parameters are given in Table I, together with their estimated uncertainties. In particular, our  $\gamma_1$  should have a very high accuracy: about  $100 \text{ cm}^{-1}$ , i.e., 3%. The uncertainty in  $\gamma_1$  comes predominantly from an unknown systematic error that we make by neglecting the renormalization of the spectrum by scattering processes. Since we assume that the imaginary part  $\Gamma \approx 65 \text{ cm}^{-1}$  of the electron self-energy due to scattering is constant, its real part has to vanish by the Kramers-Krönig relations. In fact, this real part, which is generally finite,<sup>25</sup> can shift the observed transition frequencies by an amount that scales with  $\Gamma$ .

Let us now compare our SWMc parameters with those found in previous work on bilayers and bulk graphite. For the bilayer case there is at present only one other experimental determination<sup>16</sup> of  $\gamma_j$ 's. From Table I we see that the difference between our and their values is primarily in  $\gamma_1$ . Actually, our SWMc parameters can describe the Raman data equally well<sup>46</sup> as those given in Ref. 16. Our parameter values have smaller estimated errors and should be considered more accurate.

In comparison with bulk graphite, the strongest discrepancy is in the value of  $\Delta$ . The difference is significantly larger than the uncertainty of  $\Delta_{\text{graphite}}$  quoted in



the early<sup>10,11</sup> and the recent experimental work,<sup>22</sup> which makes a strong case that  $\Delta_{\text{bilayer}}$  differs from  $\Delta_{\text{graphite}}$  both in sign and in magnitude. To judge the true significance of this result, one should recall that the physical meaning of  $\Delta_{\text{bilayer}}$  is the difference in the onsite energies of the A and B sublattices.<sup>8</sup> However, in graphite the role of the same quantity is played not by  $\Delta$  but by the linear combination<sup>9</sup>

$$\Delta'_{\text{graphite}} \equiv \Delta_{\text{graphite}} - \gamma_2 + \gamma_5. \quad (18)$$

For the sake of convenience, let us set  $\gamma_2 = \gamma_5 = 0$  in the bilayer, so that the A-B energy difference is equal to  $\Delta'$  in both materials. Taking the most commonly used<sup>10</sup> parameter values for graphite, we arrive at the remarkable empirical relation

$$\Delta'_{\text{graphite}} \approx 37 \text{ meV} \approx 2\Delta'_{\text{bilayer}}, \quad (19)$$

which is much easier to interpret. Indeed, the physical origin of  $\Delta'$  is the short-range (exponentially decaying with distance) repulsion due to exchange and correlation effects between the electron states of the stacked atoms. (Neither Coulomb nor even the van der Waals interaction have short enough range to effectively discriminate between the two sublattices,<sup>47,48</sup> given the relatively large interlayer distance.) Since in the bilayer each A atom has a single stacking partner while in the Bernal graphite it has two of them, Eq. (19) is exactly what one would expect. More precisely, it is expected if the interlayer distance in the bilayer and in the graphite are nearly the same. The validity of Eq. (19) can be considered an experimental evidence that this is indeed so.

Another SWMc constant, which may seem to be different in the bilayer and the bulk graphite is  $\gamma_4$ . As mentioned in Sec. I, this is one of the parameters that in the past have been difficult to determine very accurately. Our estimate of  $\gamma_4$  can be defended on the grounds that (i) it agrees with the Raman experiments<sup>16</sup> and (ii) it is comparable to the accepted value of  $\gamma_3$ . These two parameters describe hopping between pairs of atoms at equal distances in the lattice, see Fig. 1(a), and theoretically are not expected to be vastly different from each other. Large difference of  $\gamma_4$  between the bilayer and the bulk graphite is not expected either. Indeed, even when they disagree about the order of magnitude (or sign) of  $\Delta$ , all electronic structure calculations to date find that  $\gamma_4 \sim \gamma_3$  and are of the same order of magnitude in the two systems, see Table I.

Parameter  $\gamma_3$  itself cannot be reliably extracted from the experimental data<sup>30</sup> we analyzed here. At the relevant carrier concentrations the main effect of  $\gamma_3$  is to produce a weak trigonal warping of the band dispersion.<sup>10</sup> This warping averages out over the Fermi surface, and so has an effect similar to the broadening  $\Gamma$ : it makes the  $\gamma_1$  conductivity peak more symmetric and shifts it towards the midpoint of  $E_2$  and  $E_3$ , i.e., to slightly lower frequencies, cf. Figs. 4(a) and (b). Thus, it is difficult to separate the effect of  $\gamma_3$  from the broadening due to disorder.

Regarding the latter, the dc mobility that we find from our numerically computed  $\sigma(0)$  using  $\Gamma = 0.02\gamma_1 \approx 8 \text{ meV}$  is  $\mu \approx 3900 \text{ cm}^2/\text{Vs}$ . This is close to the transport mobility typical for bilayer graphene, supporting our interpretation that  $\Gamma$  arises mainly due to disorder.

Concluding the paper, we wish to draw attention to several features of the experimental data that are not accounted for by our model. One of them is an unexpectedly large amount of the optical weight in a range of frequencies below the  $\gamma_1$  peak. It is present between the Drude peak and  $2\mu$ , i.e., twice the chemical potential. For the chosen  $\Gamma$ , our calculation predicts  $\text{Re } \sigma(\Omega) \sim 0.02e^2/\hbar$  at such  $\Omega$ , see Fig. 3, whereas the measured value is several times larger.<sup>30</sup> This extra weight is present also in the monolayer graphene, in the same range of frequencies.<sup>42</sup> A related issue is a very gradual rise of  $\text{Re } \sigma(\Omega)$  around the point  $\Omega = 2\mu$  compared to a sharp threshold expected theoretically. These features can be in part due to electron-phonon interaction<sup>44</sup> or midgap states<sup>44,49</sup> but other effects seem to be involved as well.

One very simple explanation would be to attribute both the broadening of the  $\Omega = 2\mu$  threshold and the extra weight at  $\Omega < 2\mu$  to long-range density inhomogeneities in the sample. They can be caused by charge impurities and remnants of the photoresist used in the sample processing. The presence of such inhomogeneities would modulate the local chemical potential, and so in the infrared response one would see a certain average of the  $\sigma(\Omega)$  taken at different  $\delta V$ . We illustrate this argument by calculating the arithmetic mean of  $\sigma(\Omega)$ 's for positive (negative)  $\delta V$  and superimposing the results (shown by the dashed lines) on the  $\sigma(\Omega)$  traces for  $\delta V = +50 \text{ V}$  ( $-50 \text{ V}$ ) in Fig. 4(b). Such averaged conductivities indeed resemble the experimental data [Fig. 4(b)] more faithfully.

Another discrepancy between the experiment and the present theory is the lineshape of the  $\gamma_1$ -peak. By varying  $\Gamma$ , we can fit either the width or the height of the peak but not both. For example, in Fig. 4, where we chose to fit the width, the measured height of the peak is sometimes nearly twice larger than the theory predicts. The extra optical weight of the peaks appears to have been transferred from their high-frequency sides, which are suppressed in experiment compared to the calculations. These lineshape differences are significant enough to make us think that some essential physics is still missing in the simple single-particle picture presented in this paper. We speculate that including many-body effects may be truly necessary for bringing theory and experiment to better agreement.

We are grateful to D. Arovas, M. Dresselhaus, A. Kuzmenko, and K. Novoselov for illuminating discussions, to E. Henriksen, Z. Jiang, P. Kim, and H. L. Stormer for providing the samples, experimental assistance, and fruitful discussions and to A. Castro Neto, V. Fal'ko, and I. Martin for valuable comments on the manuscript. The work at UCSD is supported by the grants NSF DMR-

0706654, DOE DE-FG02-00ER45799, and by the UCSD ASC. The Advanced Light Source is supported by the Director, Office of Science, Office of Basic Energy Sciences, under the DOE Contract No. DE-AC02-05CH11231.

### APPENDIX A: REFLECTION AND TRANSMISSION

To compute the transmission coefficient  $T$  and the reflection coefficient  $R$  we follow the standard procedure.<sup>50</sup> In general, the result depends on the angle of incidence and on the polarization of light. Abergel and Fal'ko<sup>51</sup> derived the formulas for  $R$  and  $T$  for the  $S$ -polarization where the electric field is perpendicular to the plane of incidence (and parallel to the sample surface). We reproduce them here with a slight change in notation:

$$R = \left| \frac{C n_1 \cos \theta_1 - D [\cos \theta_0 - 4\pi\sigma]}{C n_1 \cos \theta_1 + D [\cos \theta_0 + 4\pi\sigma]} \right|^2, \quad (\text{A1})$$

$$T = \left| \frac{2 \cos \theta_0 n_1 \cos \theta_1 n_2 \cos \theta_2}{C n_1 \cos \theta_1 + D [\cos \theta_0 + 4\pi\sigma]} \right|^2,$$

where  $A$ ,  $B$ ,  $C$ , and  $D$  are given by

$$\begin{aligned} A &= \cos \theta_2 \sin \delta_2 + i n_2 \cos \theta_0 \cos \delta_2, \\ B &= i \cos \theta_2 \cos \delta_2 + n_2 \cos \theta_0 \sin \delta_2, \\ C &= A n_1 \cos \theta_2 \sin \delta_1 + i B n_2 \cos \theta_1 \cos \delta_1, \\ D &= i A n_1 \cos \theta_2 \cos \delta_1 + B n_2 \cos \theta_1 \sin \delta_1. \end{aligned} \quad (\text{A2})$$

In Eqs. (A1) and (A2), the index  $j = 0, 1, 2$  represents vacuum, SiO<sub>2</sub>, and Si layers respectively,  $n_j$  are the index of refraction of each layer, and  $\theta_j$  are the angles the light ray makes with the surface normal in each layer. They satisfy Snell's law  $n_j \sin \theta_j = \text{const}$ . Finally,  $\delta_j = kL_j/n_j$  is the phase the light picks up as it makes one pass across the layer of thickness  $L_j$ .

For the other,  $P$ -polarization, where the electric field is not exactly parallel to the surface of the sample, we find a different expression:

$$R = \left| \frac{C n_1 \cos \theta_0 - D \cos \theta_1 (1 - 4\pi\sigma \cos \theta_0)}{C n_1 \cos \theta_0 + D \cos \theta_1 [1 + 4\pi\sigma \cos \theta_0]} \right|^2, \quad (\text{A3})$$

$$T = \left| \frac{-2 \cos \theta_0 n_1 \cos \theta_1 n_2 \cos \theta_2}{C n_1 \cos \theta_0 + D \cos \theta_1 [1 + 4\pi\sigma \cos \theta_0]} \right|^2.$$

For this polarization the conductivity enters  $R$  and  $T$  multiplied by the cosine of the angle of incidence, i.e., its effect is reduced. In our experiments, we typically have  $\theta_0 \sim 30^\circ$ , and so this reduction is quite small. Its role is further diminished by the presence of both polarizations

in the infrared beam. Thus, we decided not to include it in the analysis and do all the calculation assuming the  $S$ -polarization only.

### APPENDIX B: CONDUCTIVITY OF AN UNBIASED BILAYER AT VANISHING BROADENING

The conductivity for the case  $\Gamma = V = 0$  was computed previously in Refs. 33 and 51. In our attempt to reproduce their formula we discovered that it contains a typographical sign error.<sup>52</sup> For future reference, we give the corrected expression below.

In the limit of zero broadening,  $\Gamma \rightarrow 0$ , Eqs. (14)–(17) reduce to the following expression for the conductivity:

$$\sigma(\Omega) = \frac{ge^2v^2}{2i\pi\hbar} P \int_0^\infty \frac{d\omega}{\omega} \frac{\Omega |M_{\alpha\beta}|^2}{\omega^2 - (\Omega + i0)^2} \sum_j k_j(\omega) k'_j(\omega), \quad (\text{B1})$$

where  $P$  means principal value and the integration variable  $\omega = |\varepsilon_\alpha - \varepsilon_\beta|$  is the energy difference between two states. The sum in Eq. (B1) is over all values of momentum  $k_j(\omega)$  of which two states differing in energy  $\omega$  exist. For  $V = 0$  where the the matrix elements  $M_{\alpha\beta}$  take a simple form, the integration over  $\omega$  in Eq. (B1) can be done analytically. The result can be written as a sum of three terms:

$$\frac{\sigma(\Omega)}{\sigma_0} = \tilde{\sigma}_0(\Omega) + \tilde{\sigma}_{\gamma_1}(\Omega) + \tilde{\sigma}_{2\gamma_1}(\Omega), \quad (\text{B2})$$

where  $\sigma_0 = e^2/\hbar$  is the unit of conductivity,  $\tilde{\sigma}_0$  is contribution from transitions between bands 2 and 3 that turn on at  $\Omega = 0$ ,  $\tilde{\sigma}_{\gamma_1}$  is contribution from transitions between bands 1 and 3 and bands 2 and 4 that turn on at  $\Omega = \gamma_1$ ,  $\tilde{\sigma}_{2\gamma_1}$  is contribution from transition between bands 1 and 4 that turn on at  $\Omega = 2\gamma_1$ . They are given by

$$\tilde{\sigma}_0 = \frac{g}{8} \left[ \frac{1}{2} \frac{\Omega + 2\gamma_1}{\Omega + \gamma_1} - \frac{i}{\pi} \frac{\Omega\gamma_1}{\gamma_1^2 - \Omega^2} \ln \left| \frac{\Omega}{\gamma_1} \right| \right], \quad (\text{B3a})$$

$$\tilde{\sigma}_{\gamma_1} = \frac{g}{8} \left[ \frac{\gamma_1^2}{\Omega^2} \Theta(\Omega - \gamma_1) + \frac{i}{\pi} \left( \frac{2\gamma_1}{\Omega} - \frac{\gamma_1^2}{\Omega^2} \ln \left| \frac{\gamma_1 + \Omega}{\gamma_1 - \Omega} \right| \right) \right], \quad (\text{B3b})$$

$$\begin{aligned} \tilde{\sigma}_{2\gamma_1} &= \frac{g}{8} \left[ \frac{1}{2} \frac{\Omega - 2\gamma_1}{\Omega - \gamma_1} \Theta(\Omega - 2\gamma_1) - \frac{i}{\pi} \left( \frac{1}{2} \frac{\Omega^2 - 2\gamma_1^2}{\Omega^2 - \gamma_1^2} \right. \right. \\ &\quad \left. \left. \times \ln \left| \frac{2\gamma_1 + \Omega}{2\gamma_1 - \Omega} \right| + \frac{1}{2} \frac{\Omega\gamma_1}{\Omega^2 - \gamma_1^2} \ln \left| \frac{4\gamma_1^2 - \Omega^2}{\gamma_1^2} \right| \right) \right], \end{aligned} \quad (\text{B3c})$$

where, for ease of notation,  $\Omega$  stands for  $\hbar\Omega$  and  $g = 4$ .

<sup>1</sup> K. S. Novoselov, A. K. Geim, S. V. Morozov, D. Jiang, Y. Zhang, S. V. Dubonos, I. V. Grigorieva, and A. A.

Firsov, Science **306**, 666 (2004).

<sup>2</sup> K. S. Novoselov, A. K. Geim, S. V. Morozov, D. Jiang,

- M. I. Katsnelson, I. V. Grigorieva, S. V. Dubonos, and A. A. Firsov, *Nature* **438**, 197 (2005).
- <sup>3</sup> Y. Zhang, Y. W. Tan, H. L. Stormer, and P. Kim, *Nature* **438**, 201 (2005).
- <sup>4</sup> For a review, see A. H. Castro Neto, F. Guinea, N. M. R. Peres, K. S. Novoselov, and A. K. Geim, arXiv:0709:1164; *Rev. Mod. Phys.*, in press.
- <sup>5</sup> P. R. Wallace, *Phys. Rev.* **71**, 622 (1947).
- <sup>6</sup> J. C. Slonczewski and P. R. Weiss, *Phys. Rev.* **109**, 272 (1958).
- <sup>7</sup> J. W. McClure, *Phys. Rev.* **108**, 612 (1957).
- <sup>8</sup> J. L. Carter and J. A. Krumhansl, *J. Phys. Chem.* **21**, 2238 (1953).
- <sup>9</sup> B. Partoens and F. M. Peeters, *Phys. Rev. B* **74**, 075404 (2006).
- <sup>10</sup> For a review, see M. S. Dresselhaus and G. Dresselhaus, *Adv. Phys.* **30**, 139 (1981). Reprinted as *Adv. Phys.* **51**, 1 (2002).
- <sup>11</sup> R. O. Dillon, I. L. Spain, and J. W. McClure, *J. Phys. Chem. Solids* **38**, 635 (1977).
- <sup>12</sup> For example, in the often cited<sup>16,25</sup> book of Brandt *et al.*<sup>53</sup> the sign of  $\Delta$  is shown as positive whereas the original source<sup>10,54</sup> is very clear on it being negative. Another recent review<sup>55</sup>, which is otherwise fairly up-to-date, chose nevertheless to cite an early<sup>56</sup> (later revised<sup>10</sup>) parameter determination from the MIT group.
- <sup>13</sup> R. C. Tatar and S. Rabi, *Phys. Rev. B* **25**, 4126 (1982).
- <sup>14</sup> J.-C. Charlier, X. Gonze, and J.-P. Michenaud, *Phys. Rev. B* **43**, 4579 (1991).
- <sup>15</sup> A. Grüneis, C. Attaccalite, T. Pichler, V. Zabolotnyy, H. Shiozawa, S. L. Molodtsov, D. Inosov, A. Koitzsch, M. Knupfer, J. Schiessling, et al., *Phys. Rev. Lett.* **100**, 037601 (2008).
- <sup>16</sup> L. M. Malard, J. Nilsson, D. C. Elias, J. C. Brant, F. Plentz, E. S. Alves, A. H. Castro Neto, and M. A. Pimenta, *Phys. Rev. B* **76**, 201401 (2007).
- <sup>17</sup> S. B. Trickey, F. Müller-Plathe, G. H. F. Diercksen, and J. C. Boettger, *Phys. Rev. B* **45**, 4460 (1992).
- <sup>18</sup> S. Latil and L. Henrard, *Phys. Rev. Lett.* **97**, 036803 (2006).
- <sup>19</sup> S. Latil, V. Meunier, and L. Henrard, *Phys. Rev. B* **76**, 201402 (2007).
- <sup>20</sup> H. Min, B. Sahu, S. K. Banerjee, and A. H. MacDonald, *Phys. Rev. B* **75**, 155115 (2007).
- <sup>21</sup> M. Aoki and H. Amawashi, *Solid State Commun.* **142**, 123 (2007).
- <sup>22</sup> M. Orlita, C. Faugeras, G. Martinez, D. K. Maude, M. L. Sadowski, and M. Potemski, *Phys. Rev. Lett.* **100**, 136403 (2008).
- <sup>23</sup> E. McCann and V. I. Fal'ko, *Phys. Rev. Lett.* **96**, 086805 (2006).
- <sup>24</sup> E. McCann, D. S. Abergel, and V. I. Fal'ko, *Solid State Commun.* **143**, 110 (2007).
- <sup>25</sup> J. Nilsson, A. H. Castro Neto, F. Guinea, and N. M. R. Peres, *Phys. Rev. B* **78**, 045405 (2008).
- <sup>26</sup> F. Guinea, A. H. Castro Neto, and N. M. R. Peres, *Phys. Rev. B* **73**, 245426 (2006).
- <sup>27</sup> E. V. Castro, K. S. Novoselov, S. V. Morozov, N. M. R. Peres, J. M. B. L. dos Santos, J. Nilsson, F. Guinea, A. K. Geim, and A. H. Castro Neto, *Phys. Rev. Lett.* **99**, 216802 (2007).
- <sup>28</sup> J. B. Oostinga, H. B. Heersche, X. Liu, A. F. Morpurgo, and L. M. K. Vandersypen, *Nat. Mat.* **7**, 151 (2007).
- <sup>29</sup> T. Ohta, A. Bostwick, T. Seyller, K. Horn, and E. Rotenberg, *Science* **313**, 951 (2006).
- <sup>30</sup> Z. Q. Li, E. A. Henriksen, Z. Jiang, Z. Hao, M. C. Martin, P. Kim, H. L. Stormer, and D. N. Basov, arXiv:0807.3776 (unpublished).
- <sup>31</sup> F. Wang, Y. Zhang, C. Tian, C. Girit, A. Zettl, M. Crommie, and Y. R. Shen, *Science* **320**, 206 (2008).
- <sup>32</sup> A. B. Kuzmenko, unpublished.
- <sup>33</sup> D. S. L. Abergel and V. I. Fal'ko, *Phys. Rev. B* **75**, 155430 (2007).
- <sup>34</sup> L. Benfatto, S. G. Sharapov, and J. P. Carbotte, *Phys. Rev. B* **77**, 125422 (2008).
- <sup>35</sup> E. J. Nicol and J. P. Carbotte, *Phys. Rev. B* **77**, 155409 (2008).
- <sup>36</sup> T. Ando, Y. S. Zheng, and H. Suzuura, *J. Phys. Soc. Jpn.* **71**, 1318 (2002).
- <sup>37</sup> R. R. Nair, P. Blake, A. N. Grigorenko, K. S. Novoselov, T. J. Booth, T. Stauber, N. M. R. Peres, and A. K. Geim, *Science* **320**, 1308 (2008).
- <sup>38</sup> V. P. Gusynin, V. P. Sharapov, and J. P. Carbotte, *Int. J. of Mod. Phys. B* **21**, 4611 (2007).
- <sup>39</sup> Another important source for the effective mass asymmetry is the in-plane next-nearest neighbor hopping<sup>5</sup>  $\gamma'_0 \sim 0.1\gamma_1$ . However, it does not change the optical transition energies, and so has virtually no effect on  $\sigma(\Omega)$ .
- <sup>40</sup> E. McCann, *Phys. Rev. B* **74**, 161403 (2006).
- <sup>41</sup> E. V. Castro, K. S. Novoselov, S. V. Morozov, N. M. R. Peres, J. M. B. L. dos Santos, J. Nilsson, F. Guinea, A. K. Geim, and A. H. C. Neto, arxiv:0807.3348 (unpublished).
- <sup>42</sup> Z. Q. Li, E. A. Henriksen, Z. Jiang, Z. Hao, M. C. Martin, P. Kim, H. Stormer, and D. N. Basov, *Nat. Phys.* **4**, 532 (2008).
- <sup>43</sup> Z. Q. Li, V. Podzorov, N. Sai, M. C. Martin, M. E. Gershenson, M. D. Ventra, and D. N. Basov, *Phys. Rev. Lett.* **99**, 016403 (2007).
- <sup>44</sup> T. Stauber, N. M. R. Peres, and A. H. C. Neto, *Phys. Rev. B* **78**, 085418 (2008).
- <sup>45</sup> G. D. Mahan, *Many-Particle Physics* (Plenum, New York, 1990).
- <sup>46</sup> J. Nilsson, private communication.
- <sup>47</sup> A. H. R. Palser, *Phys. Chem. Chem. Phys.* **1**, 4459 (1999).
- <sup>48</sup> A. N. Kolmogorov and V. H. Crespi, *Phys. Rev. B* **71**, 235415 (2005).
- <sup>49</sup> I. Martin, Y. M. Blanter, and A. F. Morpurgo, *Phys. Rev. Lett.* **100**, 036804 (2008).
- <sup>50</sup> J. D. Jackson, *Classical Electrodynamics* (Wiley, New York, 1998).
- <sup>51</sup> D. S. L. Abergel, A. Russell, and V. I. Fal'ko, *App. Phys. Lett.* **91**, 063125 (2007).
- <sup>52</sup> D. Abergel and V. I. Fal'ko, private communication.
- <sup>53</sup> N. B. Brandt, S. M. Chudinov, and Y. G. Ponomarev, *Semimetals I: Graphite and its Compounds* (North-Holland, Amsterdam, 1988).
- <sup>54</sup> W. W. Toy, M. S. Dresselhaus, and G. Dresselhaus, *Phys. Rev. B* **15**, 4077 (1977).
- <sup>55</sup> D. D. L. Chung, *J. Mat. Sci.* **37**, 1475 (2002).
- <sup>56</sup> M. S. Dresselhaus, G. Dresselhaus, and J. E. Fischer, *Phys. Rev. B* **15**, 3180 (1977).

